ELSEVIER

Physica D 156 (2001) 81–97

PHYSICA D

www.elsevier.com/locate/physd

A periodically forced flow displaying symmetry breaking via a three-tori gluing bifurcation and two-tori resonances

F. Marques [a], J.M. Lopez [b,*], J. Shen [c]

[a] *Departament de Física Aplicada, Universitat Politècnica de Catalunya, Jordi Girona Salgado s/n, Mòdul B4 Campus Nord, 08034 Barcelona, Spain*

[b] *Department of Mathematics, Arizona State University, Tempe, AZ 85287-1804, USA*

[c] *Department of Mathematics, University of Central Florida, Orlando, FL 32816-1364, USA*

Received 9 October 2000; received in revised form 26 February 2001; accepted 14 March 2001
Communicated by S. Fauve

Abstract

The dynamics due to a periodic forcing (harmonic axial oscillations) in a Taylor–Couette apparatus of finite length is examined numerically in an axisymmetric subspace. The forcing delays the onset of centrifugal instability and introduces a Z_2 symmetry that involves both space and time. This paper examines the influence of this symmetry on the subsequent bifurcations and route to chaos in a one-dimensional path through parameter space as the centrifugal instability is enhanced. We have observed a well-known route to chaos via frequency locking and torus break-up on a two-tori branch once the Z_2 symmetry has been broken. However, this branch is not connected in a simple manner to the Z_2-invariant primary branch. An intermediate branch of three-tori solutions, exhibiting heteroclinic and homoclinic bifurcations, provides the connection. On this three-tori branch, a new gluing bifurcation of three-tori is seen to play a central role in the symmetry breaking process.

Keywords: Periodic forcing; Taylor–Couette flow; Symmetry breaking; Gluing bifurcation; Naimark–Sacker bifurcation

1. Introduction

The Taylor–Couette flow is canonical for the study of centrifugal instabilities and the study of low co-dimension bifurcations with symmetry [8]. In the classical setting, Taylor–Couette flow is studied in the limit of infinite length cylinders and it is assumed that the flow is periodic in the axial direction. This imposes a certain symmetry group on the system, $SO(2) \times O(2)$, where the $SO(2)$ comes from the invariance to rotations about the axis and the $O(2)$ from the axial periodicity which allows invariance to continuous translations in the axial direction and to reflection about a plane orthogonal to the axis. In physical settings with annular aspect ratios of length to gap of the order of 10 times the gap or less, the presence of end walls has a profound influence on the dynamics [3,4], principally due to the change in symmetry group from $O(2)$ to Z_2 [15]. The Z_2 symmetry comes from the invariance to reflection about the mid-plane orthogonal to the axis.

In this study, we are interested in exploring the dynamics due to a periodic forcing in a Taylor–Couette setting with aspect ratio of order 10, where end-wall effects will be predominant. The particular forcing of interest here is that due to harmonic oscillations of the inner cylinder in the axial direction. Experiments [33]

* Corresponding author.
E-mail address: lopez@math.la.asu.edu (J.M. Lopez).

0167-2789/01/$ – see front matter
PII: S0167-2789(01)00261-5

have clearly demonstrated that this forcing is very efficient in postponing the onset of centrifugal instability to significantly higher rotation rates of the inner cylinder. This forcing changes the symmetry group in a subtle manner, although the symmetry group continues to be $SO(2) \times Z_2$, the Z_2 now mixes space and time. The Z_2 in the forced system is generated by the combined reflection about the mid-plane together with a half forcing period translation in time. As was pointed out some years ago [23], Z_2 is the important symmetry in the Taylor–Couette problem. Our main objective is to study how this particular form of Z_2 influences the nonlinear dynamics.

To isolate the influence of the Z_2 symmetry, we study the flow in an $SO(2)$-invariant subspace. Experiments [33] and Floquet analysis [20,21] have shown that the onset of centrifugal instability in the large aspect ratio limit is axisymmetric over an extensive range of parameter space, including the values considered in this study; in addition, the bifurcations we have found take place in a very small parameter region, close to the bifurcation point, making the assumption of axisymmetry highly plausible. Furthermore, experiments in Taylor–Couette with the same aspect ratio [6,31,32] show the presence of an axisymmetric very low frequency (VLF) mode, analogous to the three-tori we have found, although the flow is fully three-dimensional. Numerical simulations in cylindrical flows driven by rotation [17] show that the dynamics is governed by axisymmetric secondary bifurcations of the base flow, although the flows are fully three-dimensional; in this case, the nonaxisymmetric modes have less than 1% of the kinetic energy of the flow [5], and the agreement between experiments and axisymmetric simulations is impressive [27]. All these evidences provide further motivation for the restriction to an axisymmetric subspace for the present study.

In this study, we hold constant the parameters governing the geometry of the apparatus and the axial forcing, and consider a one-dimensional path through parameter space, where the rotation of the inner cylinder is progressively increased to see how the centrifugal instability manifests itself. Along the way, the Z_2 symmetry is broken and a generic route to chaos via frequency locking and torus break-up follows. The manner in which Z_2 is broken, however, is new involving heteroclinic and homoclinic bifurcations of three-tori ($\mathbb{T}^3$). In fact, the Z_2-symmetry breaking that is found corresponds to a gluing bifurcation of $\mathbb{T}^3$. This bifurcation was first reported in [16] and here, we provide a comprehensive analysis of how it plays a central role in the nonlinear dynamics of this system.

In Section 2, we describe the governing equations and symmetries of the system and the numerical techniques used. In Section 3, the primary branch which undergoes a supercritical Naimark–Sacker bifurcation is analyzed and the physical mechanism responsible for the second frequency is elucidated. In Section 4, the $\mathbb{T}^3$ branch which undergoes the gluing bifurcation and symmetry breaking is examined. The route to chaos on the secondary branch is presented in Section 5. Finally, in Section 6, an overview of how all the various branches are interrelated is presented.

2. Governing equations

The system in question is the flow between two co-axial cylinders of finite extent, the outer one being stationary and the inner one rotating at constant angular velocity Ω_i and oscillating in the axial direction with velocity $W \sin \Omega_f t$. The top and bottom end-walls are stationary. The geometry is shown schematically in Fig. 1. The radii of the cylinders are r_i and r_o (inner and outer, respectively), and their length is L; the annular gap between the cylinders is $d = r_o - r_i$. These parameters are combined to give the following

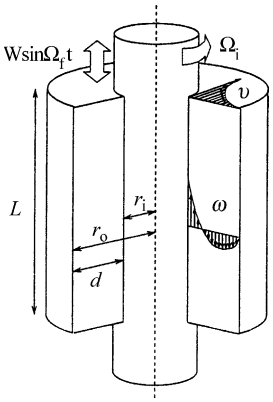

Fig. 1. Schematic representation of the flow configuration.

nondimensional governing parameters: the radius ratio, $e = r_i/r_o$; the aspect ratio, $\Lambda = L/d$; the Couette flow Reynolds number, $Ri = dr_i\Omega_i/\nu$; the axial Reynolds number, $Ra = dW/\nu$; the nondimensional frequency, $\omega_f = d^2\Omega_f/\nu$, where ν is the kinematic viscosity of the fluid.

The length and time scales used are the gap, d, and the diffusive time across the gap, d^2/ν, respectively. With these scalings, the Navier–Stokes equations and the incompressibility condition become

$$\partial_t \mathbf{v} + (\mathbf{v}\cdot\boldsymbol{\nabla})\mathbf{v} = -\boldsymbol{\nabla} p + \Delta\mathbf{v}, \quad \boldsymbol{\nabla}\cdot\mathbf{v} = 0. \tag{1}$$

The boundary conditions are no-slip on all walls. This leads to discontinuous boundary conditions for the axial and azimuthal components of velocity where the moving inner cylinder meets the stationary top and bottom end-walls. These discontinuities in a physical experiment correspond to a small, but finite gap (see for example, Refs. [27,33]) and in Section 2.2, we describe how this is treated numerically.

The basic flow is time-periodic with period $T_f = 2\pi/\omega_f$ and synchronous with the forcing, and it is independent of the azimuthal coordinate. The imposed periodic forcing in this problem implies the existence of a global Poincaré map, $\boldsymbol{P}$, i.e. strobing with the forcing frequency ω_f.

2.1. Symmetry considerations

The Navier–Stokes equations governing this problem are invariant under rotations of angle α, R_α, around the common axis of the cylinders, generating the symmetry group $SO(2)$. Moreover, the equations are invariant under an additional discrete symmetry, S, involving time and the axial coordinate; it is a reflection about the mid-plane orthogonal to the axis with a simultaneous time-translation of a half period. Using cylindrical coordinates, they read

$$(R_\alpha \mathbf{v})(r,\theta,z,t) = \mathbf{v}(r,\theta+\alpha,z,t), \quad \alpha \in \mathbb{R} \mod 2\pi, \tag{2}$$

$$(S\mathbf{v})(r,\theta,z,t) = (u,v,-w)\left(r,\theta,-z,t+\tfrac{1}{2}T_f\right) \tag{3}$$

where $\mathbf{v}$ is the velocity field and (u, v, w) are the components in cylindrical coordinates. The symmetry S satisfies $S^2 = I$, and the symmetry group of our problem is $SO(2) \times Z_2$. The $SO(2)$ factor comes from R_α and the Z_2 factor is generated by S.

The basic state, a limit cycle, is invariant under the full symmetry group of the equations, $SO(2) \times Z_2$. It can lose stability when at least one Floquet multiplier λ crosses the unit circle. In general, this may occur through $\lambda = +1$ (synchronous bifurcation), $\lambda = -1$ (subharmonic bifurcation) or a pair of complex conjugate multipliers cross (Naimark–Sacker bifurcation). In a system without symmetries, the $\lambda = +1$ case corresponds to the saddle-node bifurcation, the $\lambda = -1$ case corresponds to a period doubling and the complex conjugate case is the Naimark–Sacker bifurcation. However, when the Z_2 symmetry group is present, it inhibits the period doubling ($\lambda = -1$) bifurcation [29], the synchronous bifurcation becomes a pitchfork and the Naimark–Sacker bifurcation results in a Z_2-invariant $\mathbb{T}^2$ [14].

In this study, we solve the system in an axisymmetric subspace invariant to $SO(2)$. Linear stability analyses in the limit $\Lambda \to \infty$, as well as experiments with $\Lambda = 150$ have shown that over an extensive range of parameter space, the primary bifurcation is to an axisymmetric state, periodic in the axial direction and synchronous with the forcing, and only in small windows of parameter space have nonaxisymmetric flows been observed [20,21,33]. Therefore, the only nontrivial symmetry of the axisymmetric system considered is S.

2.2. Numerical solution technique

The nonlinear axisymmetric Navier–Stokes equations (1) are solved employing a highly efficient and accurate spectral-projection method [19] in which the time variable is discretized by using a second-order projection scheme [25,30] and the spatial variables are discretized by using a spectral-Galerkin method [24,26].

The flow starts either from rest or as a continuation from a solution with different parameter values and satisfies the following boundary conditions:

$$u = 0, \quad v = Ri, \quad w = Ra\sin\omega_f t \ \text{ at } \ r = r_i,$$
$$u = v = w = 0 \ \text{ at } \ r = r_o \ \text{ and } \ z = \pm\tfrac{1}{2}\Lambda. \tag{4}$$

This flow has discontinuous boundary conditions for the azimuthal, v, and axial, w, components of velocity where the inner cylinder meets the stationary end-walls. Since spectral methods are very sensitive to the smoothness of the solutions, it is crucial to design a sensible treatment for the discontinuous boundary conditions. This discontinuity is a mathematical idealization of the physical situation (a small finite gap). Therefore, it is appropriate to use a regularized boundary layer function to approximate the actual physical situation. In fact, the discontinuous boundary conditions at $z = \pm\frac{1}{2}\Lambda$

$$v = 0 \quad \text{for } r \in (r_\mathrm{i}, r_\mathrm{o}] \quad \text{and} \quad v = Ri \quad \text{at } r = r_\mathrm{i},$$

and

$$w = 0 \quad \text{for } r \in (r_\mathrm{i}, r_\mathrm{o}] \quad \text{and}$$
$$w = Ra \sin \omega_\mathrm{f} t \quad \text{at } r = r_\mathrm{i}$$

can be approximated, respectively, by

$$v_\varepsilon(r) = Ri \exp\left(-\frac{r - r_\mathrm{i}}{\varepsilon}\right), \quad r \in [r_\mathrm{i}, r_\mathrm{o}], \tag{5}$$

and

$$w_\varepsilon(r) = Ra \sin \omega_\mathrm{f} t \exp\left(-\frac{r - r_\mathrm{i}}{\varepsilon}\right), \quad r \in [r_\mathrm{i}, r_\mathrm{o}] \tag{6}$$

to within any prescribed accuracy by choosing an appropriate ε. Such an approach has been proven successful in [19] for treating the discontinuous boundary condition for the v component. Numerical modeling of the corner singularity for the Taylor problem has been discussed previously in [10] using a different numerical method.

In this study, the axisymmetric Navier–Stokes equations have been solved with the spectral scheme described in [18], using 80 axial and 64 radial modes, and a time-step $\delta t = \frac{1}{200} T_\mathrm{f}$. With 64 modes in the radial direction, we were able to use $\varepsilon = 0.005$ in (5) and (6), which corresponds to the physical separation between the end-wall and side wall in typical experiments with $d \sim 1\,\mathrm{cm}$. Note that further reducing ε without increasing the radial resolution would introduce unwanted oscillations. We only consider variations in Ri, keeping all other parameters fixed ($\Lambda = 10$, $e = 0.905$, $Ra = 80$, $\omega_\mathrm{f} = 30$).

For axisymmetric flows in cylindrical geometries, it is typical to present the solutions in terms of the streamfunction ψ, the azimuthal component of vorticity η and the axial component of the angular momentum $\gamma = rv$. The velocity vector can be written as

$$\mathbf{v} = (u, v, w) = \left(-\frac{1}{r}\frac{\partial \psi}{\partial z}, \frac{\gamma}{r}, \frac{1}{r}\frac{\partial \psi}{\partial r}\right),$$

and the vorticity vector as

$$\boldsymbol{\nabla} \times \mathbf{v} = \left(-\frac{1}{r}\frac{\partial \gamma}{\partial z}, \eta, \frac{1}{r}\frac{\partial \gamma}{\partial r}\right),$$

where

$$\eta = \frac{\partial u}{\partial z} - \frac{\partial w}{\partial r} = -\frac{1}{r}\left(\frac{\partial^2 \psi}{\partial z^2} + \frac{\partial^2 \psi}{\partial r^2} - \frac{1}{r}\frac{\partial \psi}{\partial r}\right). \tag{7}$$

We solve the governing equations using velocity and pressure, and then the azimuthal vorticity η is found by spectral differentiation of u and w, the stream function ψ is found by solving the Helmholtz equation (7) and γ by spectral multiplication of rv. Note that in a meridional plane (r, z), contours of ψ are projections of the streamlines and contours of γ are projections of the vortex lines.

3. The primary branch

In this section, we describe the dynamics along the primary branch, the branch of solutions that is smoothly connected to the basic state at $Ri = 0$. This basic state corresponds essentially to an annular Stokes flow, the annular analogue of the flow driven by the in-plane harmonic oscillation of a plate [28], but is modified by: (i) the presence of end-walls and (ii) the outer cylinder. The presence of these walls enforces a zero mass flux, so that on the up (down) stroke of the inner cylinder there is a return flow down (up) the outer cylinder. Most of the features of the basic state are common to the limiting case $\Lambda \to \infty$ [20], but here the end-walls will be shown to play a significant role in the subsequent dynamics of the flow as Ri is increased.

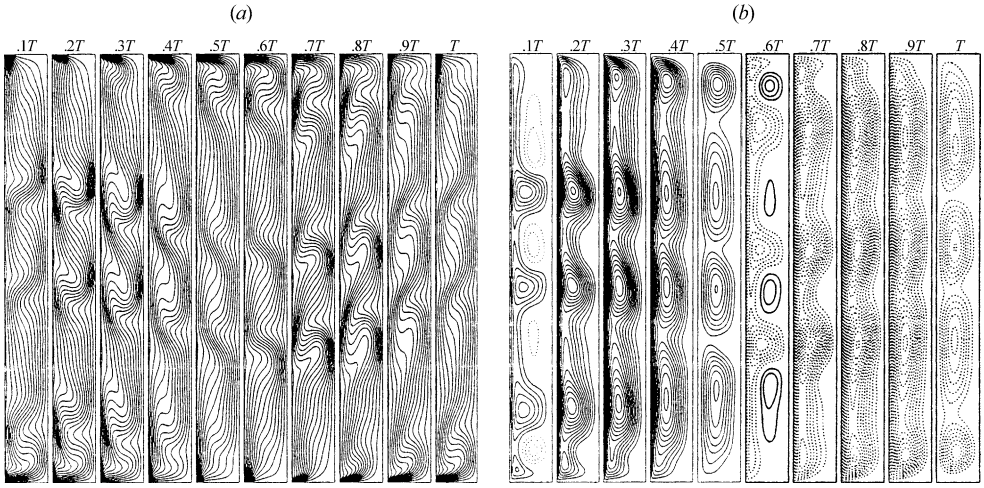

Fig. 2. Contours depicting: (a) vortex lines and (b) streamlines at 10 equispaced phases over one complete forcing period T for the $\mathbb{T}^1$ solution on the primary branch for $Ri = 280.0$.

In the limiting case $\Lambda \to \infty$, increase in Ri led to centrifugal instability of the basic state, however, the presence of end-walls separated by a finite distance leads to a smooth transition. In the $\Lambda \to \infty$ case, the bifurcation is a pitchfork of revolution and the bifurcating solutions differ in phase (a spatial translation along the axis). In fact, in most numerical settings, a planar pitchfork is obtained because the phase is fixed except for a π shift (a sign in the amplitude); a detailed discussion, both theoretical and experimental in the Taylor–Couette problem can be found in [9]. The presence of end-walls generates a z-dependent flow close to the end-walls that progressively fills the whole domain when Ri is increased. At finite Ri, the flow on the primary branch is characterized by the presence of jets emanating from the inner cylinder boundary layer that advect the vortex lines into the interior (see Fig. 2(a)) and associated with these jets, the streamlines have a cellular structure reminiscent of Taylor vortices (see Fig. 2(b)). The jets are dragged up and down by the motion of the inner cylinder, synchronous with the forcing. This basic state is a limit cycle ($\mathbb{T}^1$) and retains all the symmetries of the system.

When Ri is increased beyond a critical value, a Naimark–Sacker bifurcation [14] leads to flow on a $\mathbb{T}^2$. The basic state, being a $\mathbb{T}^1$, is a point in the Poincaré section whereas the $\mathbb{T}^2$ is a closed loop in $\boldsymbol{P}$. Fig. 3(a) shows the Poincaré sections of the solutions for $Ri = 280.1$–280.8 in steps of 0.1. $Ri = 280.1$ is before the supercritical Naimark–Sacker bifurcation. The amplitudes of the loops corresponding to the $\mathbb{T}^2$ scales with $\sqrt{Ri - Ri_c}$, where Ri_c is the critical Ri at the bifurcation. In Fig. 3(b), these amplitudes and the corresponding fit are shown, and allow an estimate of $Ri_c = 280.188$. The phase portraits are in the (Γ, U) plane, where Γ and U are the γ and u evaluated at a convenient Gauss–Lobato point in the annulus ($r = r_i + 0.573$, $z = 0.969$).

Although resonance horns (Arnold's tongues) are often associated with Naimark–Sacker bifurcations, over the range of Ri where the $\mathbb{T}^2$ bifurcating from the primary $\mathbb{T}^1$ branch is stable, we have not observed any intervals of frequency locking. On the $\mathbb{T}^2$, one frequency is fixed, determined by the forcing frequency $\omega_f = 30$, and the second frequency, ω_s, varies with Ri in the range 5.2–5.4. So, the bifurcated solutions are quasi-periodic and hence are not S-invariant. However, the $\mathbb{T}^2$ on which the solutions reside is S-invariant; we have taken a bifurcated solution, applied the S symmetry, and found that this transformed solution resides on the same $\mathbb{T}^2$. Naimark–Sacker bifurcations in ODE systems with Z_2 symmetry (not involving time)

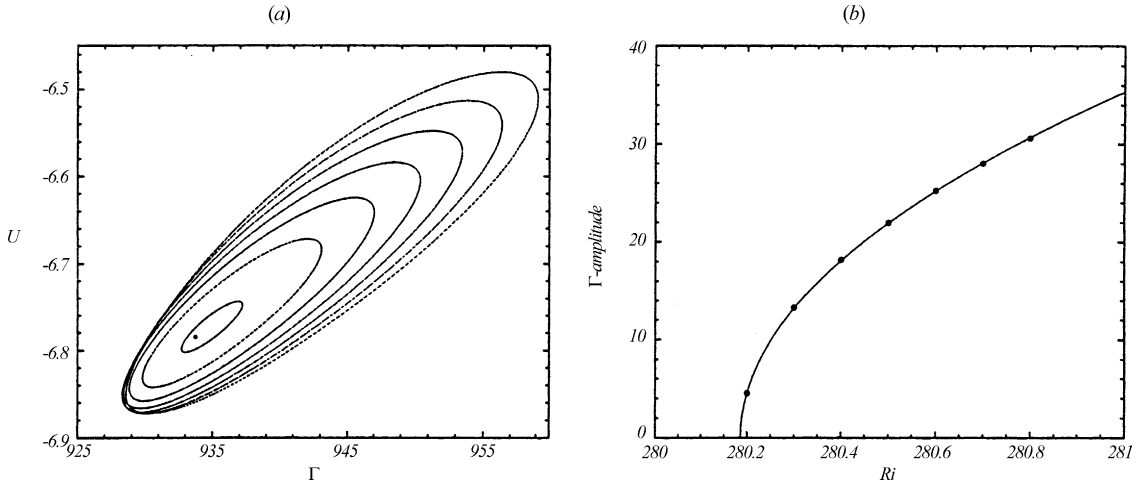

Fig. 3. Poincaré sections of the solutions on the primary branch depicting the $\mathbb{T}^1$ solution at $Ri = 280.1$ as a point and the successive $\mathbb{T}^2$ solutions for $Ri = 280.2 + 0.1n$ with $n \in [0, 6]$ as the cycles with amplitude increasing with Ri and (b) variation of the amplitudes in (a) with Ri.

always result in an Z_2-invariant $\mathbb{T}^2$ [14]. Our Z_2 generated by S does involve time, yet we observe the same behavior (an invariant $\mathbb{T}^2$ following the bifurcation) in our system.

To determine what the second frequency, ω_s, corresponds to, we have strobed the streamfunction at the forcing frequency. Fig. 4 shows these strobed images over 10 forcing periods. A $\mathbb{T}^1$ solution would be constant in such a sequence. The $\mathbb{T}^2$ solution shows variations that are concentrated in the top and bottom thirds of the cylinder while the central third does not change. This suggests that ω_s corresponds to an unsteady coupling between the end-wall vortices and the jets emanating from the boundary layer on the inner cylinder. This is further discussed when comparing the flows on other branches in Section 5.

The $\mathbb{T}^2$ solution branch bifurcating from the primary branch at $Ri = 280.188$ ceases to be stable beyond $Ri = 280.88$. Attempts to continue the $\mathbb{T}^2$ solution branch beyond $Ri = 280.88$ result in an evolution to a three-torus ($\mathbb{T}^3$) solution. The theoretical study of bifurcations of tori is difficult, some scenarios have been rigorously analyzed by generalizing Floquet theory in systems without symmetries [7]. To our knowledge, no such studies with Z_2 symmetry have been published.

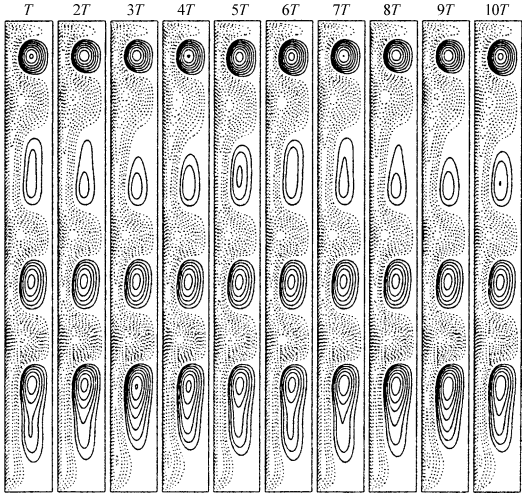

Fig. 4. Streamlines of a solution on the primary branch with $Ri = 280.88$, strobed over 10 periods at a fixed phase. Thirty contour levels in the range $[-75, 75]$ are used, solid (broken) lines indicate positive (negative) contour levels.

4. Three-tori branch

We have located a range ($Ri \in [280.89, 281.26]$) where stable $\mathbb{T}^3$ solutions exist. Their characteristics are elucidated with the aid of the global Poincaré map $\boldsymbol{P}$, time series and phase portraits in the (Γ, U) plane.

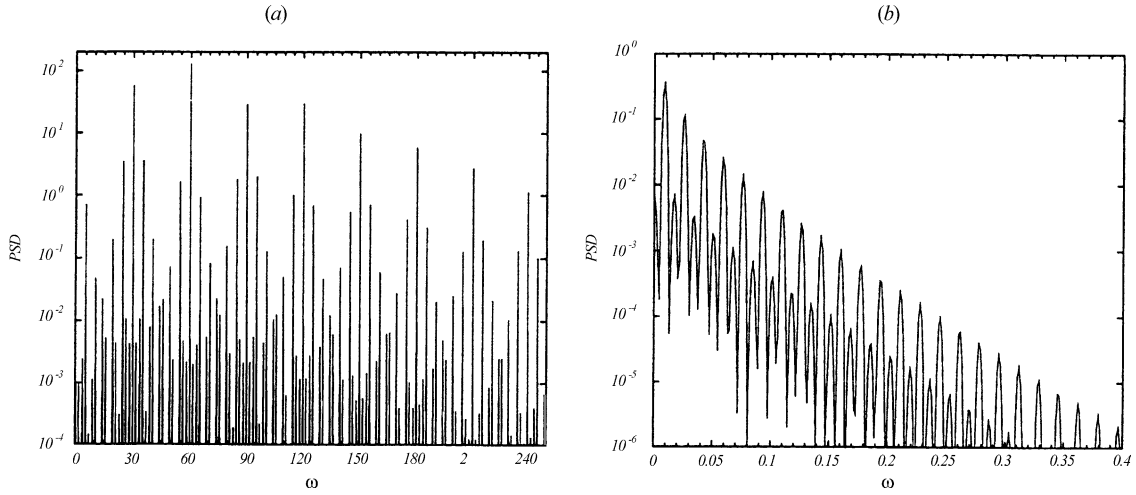

Fig. 5. (a) Power spectra of a $\mathbb{T}^3$ solution at $Ri = 280.98$, and (b) a zoom of the PSD in (a) near the origin.

The power spectral density (PSD) of the time series of Γ, shown in Fig. 5(a), has a main peak at the forcing frequency, $\omega_f = 30$, a second frequency at $\omega_s \approx 5.2$, and their linear combinations since these are incommensurate. This second frequency is very close to ω_s of the $\mathbb{T}^2$ on the primary branch following the Naimark–Sacker bifurcation. The PSD also possesses a VLF, ω_{VLF}, which is three orders of magnitude smaller than ω_s. Fig. 5(b) is a zoom of (a) near the origin showing the peak at ω_{VLF} and its harmonics. Due to the large spectral gaps between these three incommensurate frequencies, we have been able to unambiguously characterize these solutions as $\mathbb{T}^3$.

Over the range of Ri where $\mathbb{T}^3$ solutions exist, $\omega_s = 5.2 \pm 3\%$. In contrast, $T_{VLF} = 2\pi/\omega_{VLF}$ experiences dramatic changes over this range, as shown in Fig. 6. This figure indicates that there are two Ri values where T_{VLF} becomes unbounded. For ease of discussion, we now represent $\mathbb{T}^3$ as limit cycles and $\mathbb{T}^2$ as fixed points. This analogy works since the two suppressed frequencies, ω_f and ω_s are almost constant (in fact, ω_f is constant), over the range of Ri of interest and they do not play an essential role in the dynamics near the bifurcation points. Infinite-period bifurcations are usually associated with homoclinic or heteroclinic behavior. The two most typical are the following: (i) a limit cycle collides with a hyperbolic fixed point resulting in a homoclinic connection and then vanishes; (ii) a saddle-node occurs on the limit cycle. These two scenarios are distinguished by the asymptotic behavior of the period of the limit cycle as the bifurcation point is approached. In case (i), the period close to the bifurcation point would have the form [12]

$$T_{VLF} \sim \lambda_{hom}^{-1} \ln\left(\frac{1}{|Ri - Ri_{crit}|}\right) + d, \tag{8}$$

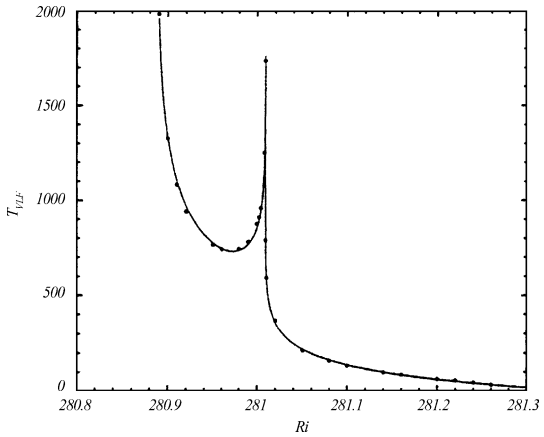

Fig. 6. Variation of $T_{VLF} = 2\pi/\omega_{VLF}$ with Ri. Symbols are computed values and solid lines are log fits.

while in case (ii) it has the form [14]

$$T_{\mathrm{VLF}} \sim \frac{c}{\sqrt{|Ri - Ri_{\mathrm{crit}}|}} + d.$$

Our computed T_{VLF} fits the logarithmic form very well, whereas it does not adjust to the square root form. The fitted logarithmic curves are the solid lines in Fig. 6 and the symbols are the computed periods. The fits are uniformly good over the whole range of existence of the $\mathbb{T}^3$, strongly suggesting that the homoclinic/heteroclinic behavior dominates the dynamics over the whole interval. The expression for the logarithmic profile in the first section is given by

$$T_{\mathrm{VLF}} = \lambda_{\mathrm{het}}^{-1} \ln \frac{1}{|Ri - Ri_{\mathrm{het}}|} + \lambda_{\mathrm{hom}}^{-1} \ln \frac{1}{|Ri - Ri_{\mathrm{hom}}|} + c.$$

In the entire second section, the logarithmic fit (8) was used. The logarithmic fits give the critical Ri for the two infinite period bifurcations, $Ri_{\mathrm{het}} = 280.88736$ and $Ri_{\mathrm{hom}} = 281.00884$. The factors λ_{het} and λ_{hom} are the eigenvalues corresponding to the unstable direction of the hyperbolic fixed points [12], in our case these are unstable $\mathbb{T}^2$. The values obtained are $\lambda_{\mathrm{het}} = 2.43 \times 10^{-3}$ and $\lambda_{\mathrm{hom}} = 5.81 \times 10^{-3}$.

Fig. 7 shows the iterates of Γ under the map $\boldsymbol{P}$ (for brevity, we shall refer to these as time series of $\boldsymbol{P}(\Gamma)$) and phase portraits in the (Γ, U) plane. These are given at three values of Ri, each close to the infinite period bifurcation points depicted in Fig. 6. Fig. 7(a) corresponds to $Ri = 280.89$, the closest Ri value to Ri_{het} computed. The time series shows that the solution trajectory spends a long time close to not one, but two unstable $\mathbb{T}^2$ with rapid excursions between them; this behavior is also apparent in the phase portrait. The two unstable $\mathbb{T}^2$ appear as two cycles and the trajectory in the phase portrait spends a long time near them. The rapid excursions appear as tubular manifolds connecting them. As $Ri \to Ri_{\mathrm{het}}^{+}$, the $\mathbb{T}^3$ depicted in Fig. 7(a) becomes a heteroclinic three-manifold. This is illustrated schematically in Fig. 8. In this figure, $\mathbb{T}^2$ are represented by fixed points and $\mathbb{T}^3$ by limit cycles, the bold (thin) cycles being (un)stable. The $\mathbb{T}^3$ is S-invariant, whereas the pair of unstable $\mathbb{T}^2$ to which it connects heteroclinically at Ri_{het} are not, but are related to each other via the S symmetry. The $\mathbb{T}^3$ collides with the two unstable $\mathbb{T}^2$ simultaneously due to the S symmetry.

The infinite period bifurcation at $Ri = Ri_{\mathrm{hom}}$ is more complicated as $\mathbb{T}^3$ exist on both sides of the bifurcation. Approaching Ri_{hom} from below, the $\mathbb{T}^3$ is S-invariant and approaches an unstable $\mathbb{T}^2$ which is also S-invariant. This is seen in the time series and the phase portrait (Fig. 7(b)) for $Ri = 281.008$, which is very close to Ri_{hom}. The figure shows the presence of two distinct fast homoclinic excursions. At the bifurcation point, Ri_{hom}, there exists two homoclinic loops that are related by the S symmetry. This is also illustrated schematically in Fig. 8.

For $Ri > Ri_{\mathrm{hom}}$, but close to the bifurcation, the behavior is qualitatively different. Fig. 7(c) shows at $Ri = 281.009$, the existence of a $\mathbb{T}^3$ close to an unstable $\mathbb{T}^2$ with a single homoclinic excursion. We also note from Fig. 6 that for $Ri > Ri_{\mathrm{hom}}$, the period T_{VLF} is significantly reduced from that when $Ri < Ri_{\mathrm{hom}}$. Beyond Ri_{hom}, the double homoclinic loop splits into two $\mathbb{T}^3$ as shown in the schematic Fig. 8. The solution in Fig. 7(c) corresponds to one of these $\mathbb{T}^3$, which is no longer S-invariant. We have explicitly computed the S-related partners for $Ri > Ri_{\mathrm{hom}}$ by applying the symmetry S to a trajectory on the first obtained $\mathbb{T}^3$, a trajectory on a different $\mathbb{T}^3$ results. These two distinct $\mathbb{T}^3$ are S-symmetrically related. We have not been able to continue the $\mathbb{T}^3$ solution branches beyond $Ri = 281.26$; the system evolves to another one corresponding to a $\mathbb{T}^2$ branch that is described in Section 5.

The range of Ri where $\mathbb{T}^3$ exist consists of two branches, for $Ri_{\mathrm{het}} < Ri < Ri_{\mathrm{hom}}$ there is a single S-invariant $\mathbb{T}^3$ and for $Ri > Ri_{\mathrm{hom}}$ a pair of non-symmetric, but symmetrically related, $\mathbb{T}^3$. The first branch starts in a heteroclinic bifurcation schematically shown in Fig. 8 and is related to the second branch via a homoclinic bifurcation at $Ri = Ri_{\mathrm{hom}}$. In this homoclinic bifurcation an S-invariant $\mathbb{T}^3$ splits in two S-related $\mathbb{T}^3$. Analogous gluing bifurcations of limit cycles in systems with Z_2 symmetry have been analyzed in [13] and in [1] for systems with more complex (D_4) symmetries. Here, we have a gluing bifurcation of $\mathbb{T}^3$ in a real fluid system.

From Fig. 8, we see that three unstable $\mathbb{T}^2$ play a key role as organizing centers for the dynamics of the

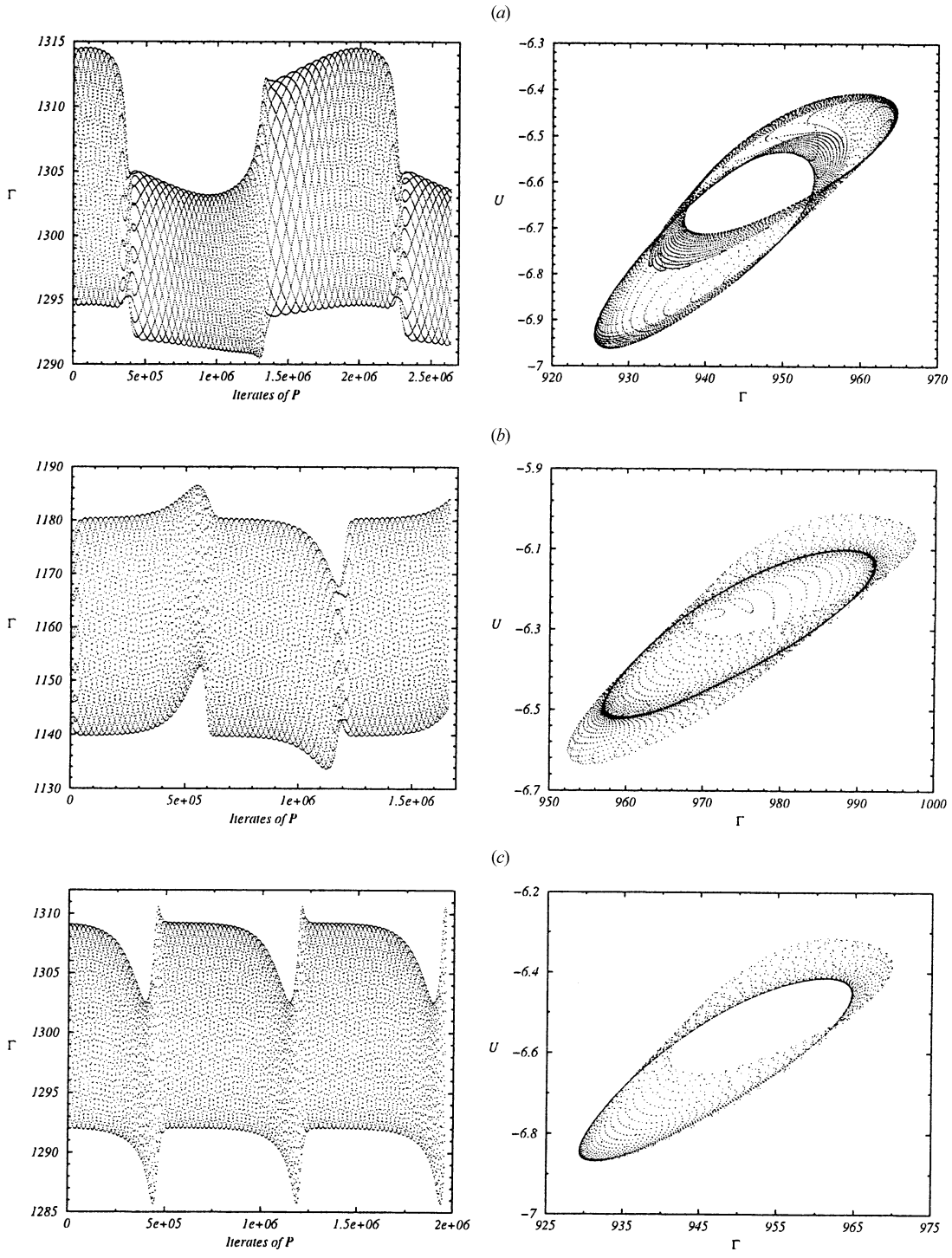

Fig. 7. Time series of $\boldsymbol{P}(\Gamma)$ (left) and phase portraits in the (Γ, U) plane (right) for $Ri = 280.89$ (a), 281.008 (b), 281.008 (b), 281.009 (c).

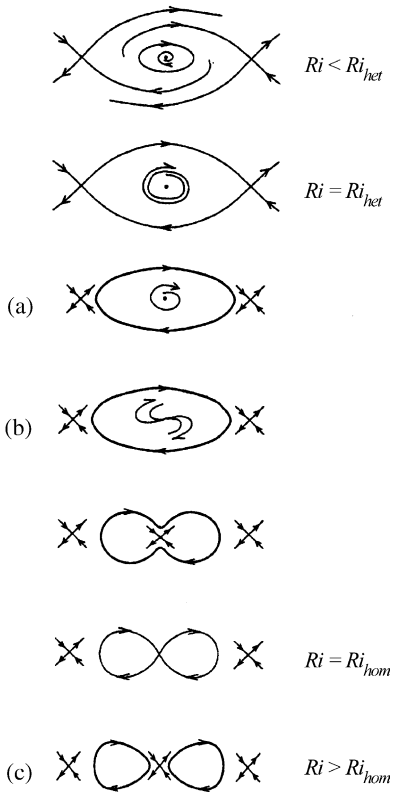

Fig. 8. Schematic representation of the bifurcation sequence for the $\mathbb{T}^3$ solutions. In this schematic representation, $\mathbb{T}^2$ are represented as fixed points and $\mathbb{T}^3$ as cycles. The labels (a), (b) and (c) correspond to the three parts of Fig. 7.

stable $\mathbb{T}^3$. The unstable $\mathbb{T}^2$ in the center of Fig. 8 is S-invariant since it is central to the gluing bifurcation. Further, ω_s is continuous along the primary branch and the $\mathbb{T}^3$ branches, with the connection between these branches occurring at the homoclinic point Ri_{hom}.

We are able to explore the flow characteristics associated with the S-invariant unstable $\mathbb{T}^2$ at points in parameter space where the stable $\mathbb{T}^3$ is almost homoclinic to it, i.e. $Ri \approx Ri_{\text{hom}}$. From Fig. 7(b), we see that for approximately 3×10^5 iterates of $\boldsymbol{P}$, the $\mathbb{T}^3$ remains very close to the unstable $\mathbb{T}^2$. In Fig. 9, we show streamlines at 10 consecutive iterates of $\boldsymbol{P}$, starting after the first 10^5 iterates in Fig. 9. Note that since $\omega_s \approx 5.28$, this sequence almost repeats itself every $\omega_f/\omega_s \approx 5.7$ iterates of $\boldsymbol{P}$ for the subsequent 2×10^5 iterates of $\boldsymbol{P}$. Fig. 9 displays the same behavior as

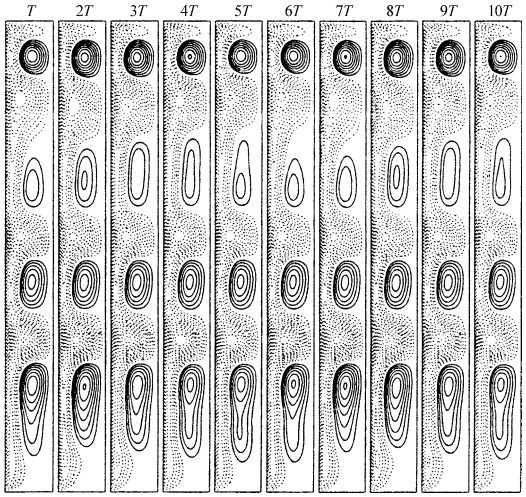

Fig. 9. Streamlines of a solution on the primary branch with $Ri = 281.008$, while it is close to the unstable symmetric $\mathbb{T}^2$ at indicated multiples of the forcing period; contours levels as in Fig. 4.

that in Fig. 4 which corresponds to the stable $\mathbb{T}^2$ on the primary branch. This suggests that the unstable $\mathbb{T}^2$ and the stable $\mathbb{T}^2$ are on the same S-invariant solution branch (the primary branch).

For $Ri \approx Ri_{\text{het}}$, since the $\mathbb{T}^3$ passes close to two unstable $\mathbb{T}^2$ and remains close to them for long time (about 5×10^5 iterates of $\boldsymbol{P}$), we are also able to explore the flow characteristics associated with these $\mathbb{T}^2$. Fig. 10 shows the streamlines at 10 consecutive iterates of $\boldsymbol{P}$; part (a) corresponds to times when the $\mathbb{T}^3$ is close to one of the unstable $\mathbb{T}^2$ and (b) to the other. The behavior is very similar to that in Fig. 9, showing the modulation due to ω_s as oscillations near both end-walls, the difference between each of the three cases is in the phase difference between the oscillations near the top and bottom end-walls.

We have not been able to continue the $\mathbb{T}^3$ beyond $Ri > 281.26$; the system evolves to another far off branch that is described in the next section.

5. A route to chaos through resonance horns

The branch to be described here is robust in the sense that time evolution from an initial state of rest evolves to this branch, even for Ri values for which

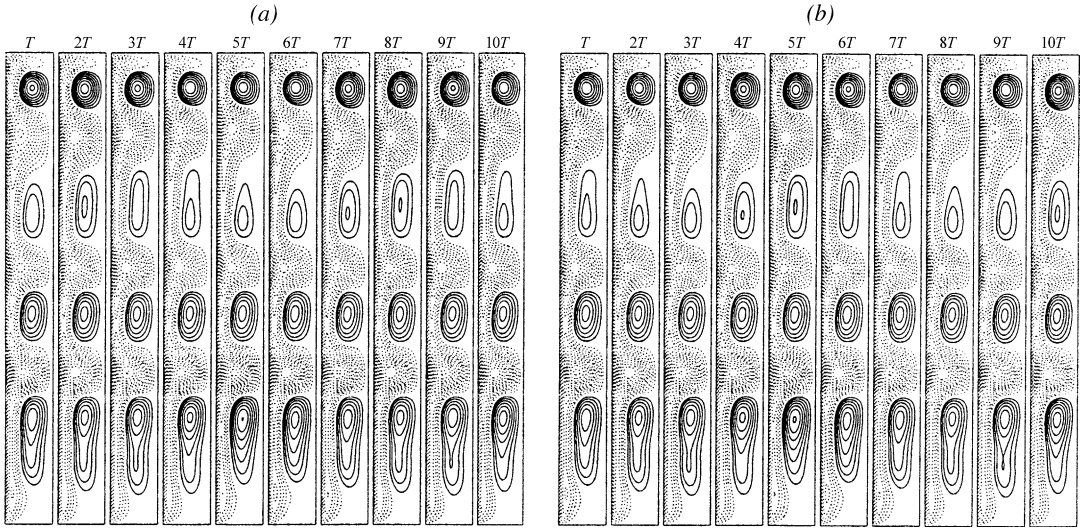

Fig. 10. Streamlines of a solution on the $\mathbb{T}^3$ branch for $Ri = 280.89$ while it is close to the: (a) unstable nonsymmetric $\mathbb{T}^2$ and (b) its symmetric counter part, at indicated multiples of the forcing period; contours level as in Fig. 4.

the primary and the $\mathbb{T}^3$ branches coexist and are stable. We have been able to continue this branch, which we shall denote as the secondary branch, down to $Ri = 280.46$. For $Ri < 280.46$, the attempts to continue this branch led to evolutions onto the primary $\mathbb{T}^2$ branch.

The main distinction between this secondary $\mathbb{T}^2$ branch and the primary $\mathbb{T}^2$ branch described in Section 3 is that the $\mathbb{T}^2$ here is not S-invariant. This is readily determined by taking a solution on this branch, applying the S-symmetry and observing that the resultant solution trajectory resides on a different $\mathbb{T}^2$. We

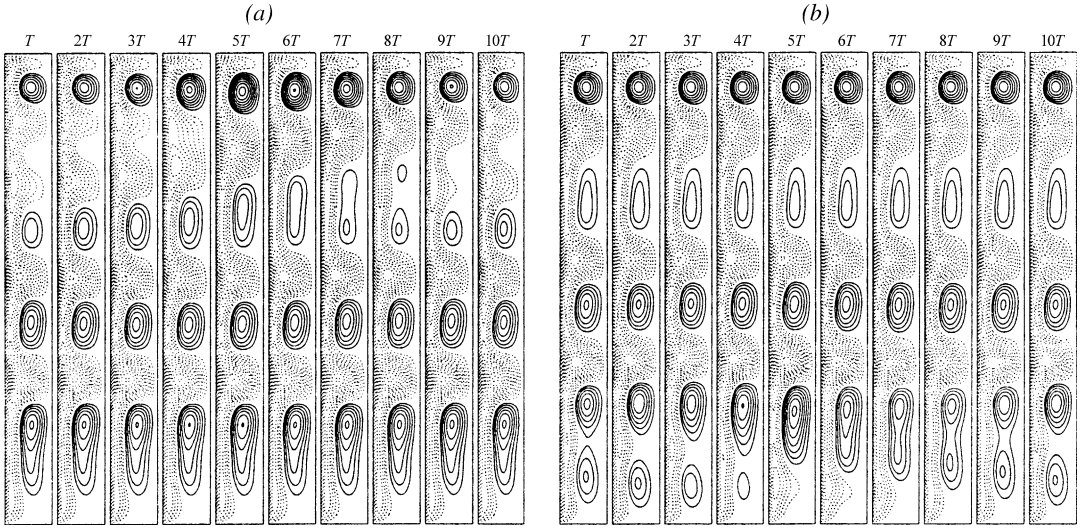

Fig. 11. Streamlines, at $Ri = 280.9$, strobed at a fixed phase of the forcing at indicated multiples of the forcing period for a solution on: (a) the secondary branch; (b) its S-related solution branch, contours level as in Fig. 4.

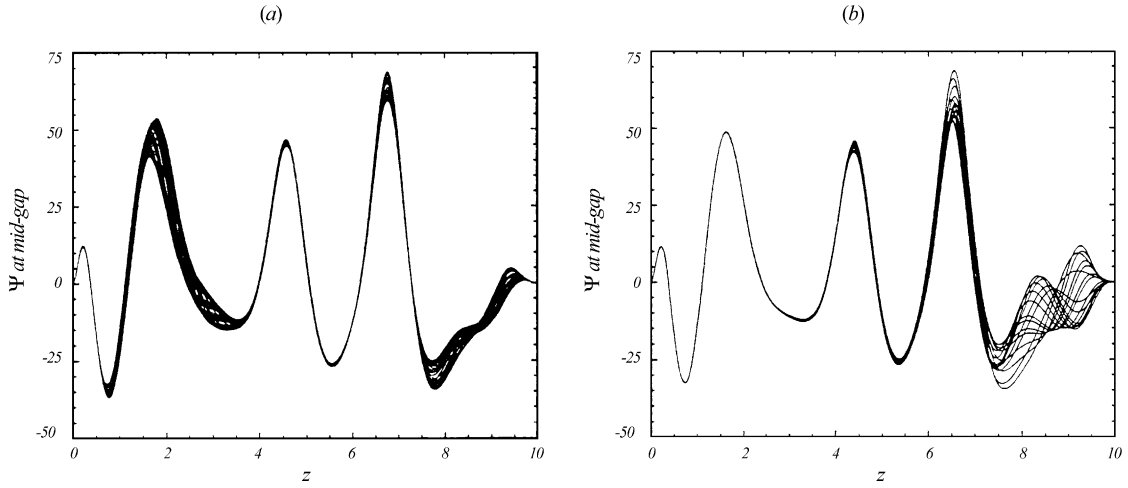

Fig. 12. Profiles of ψ at the mid-gap, $r = \frac{1}{2}(r_o + r_i)$, strobed at the forcing frequency and all at the same phase: (a) corresponds to the stable $\mathbb{T}^2$ shown in Fig. 4 and the unstable $\mathbb{T}^2$ in Figs. 9 and 10; (b) corresponds to the stable $\mathbb{T}^2$ shown in Fig. 11(a).

have done this for several Ri, the particular case $Ri = 280.9$ is illustrated in Fig. 11, showing the streamlines strobed at consecutive iterates of $\boldsymbol{P}$ along with the S-related solution.

The flow characteristics on this branch differ from those on the primary and $\mathbb{T}^3$ branches in three main features. First, the modulations due to ω_s are confined to one of the end-wall regions rather than having oscillations near both end-walls. Fig. 12 illustrates this by showing the profiles of ψ at the mid-gap, $r = \frac{1}{2}(r_o + r_i)$, strobed at the forcing frequency and all at the same phase for the $\mathbb{T}^2$ shown in Fig. 4 (stable symmetric on primary branch), 10 (unstable nonsymmetric on the $\mathbb{T}^3$ branch) and nine (unstable symmetric on the $\mathbb{T}^3$ branch), and contrasts them with the ψ profiles for the $\mathbb{T}^2$ in Fig. 11(a) (stable nonsymmetric on the secondary branch). Second, the modulations have a traveling wave characteristic rather than being pulsations and third, ω_s is substantially smaller (≈ 3.5 rather than ≈ 5.2). The distinction between the two S-related secondary branches is exemplified in Fig. 11, where it is seen that on one branch the ω_s modulations occur near the top end-wall and on the other it is near the bottom end-wall. For the rest of this section, we shall describe how the dynamics of one of the secondary branches evolves with increasing Ri.

The one-dimensional path through parameter space that we follow on the secondary branch reveals the characteristics of a quasi-periodic Ruelle–Takens route to chaos. The Ruelle–Takens scenario requires two parameters to describe its complete dynamics. Generically, there is a curve in this two-dimensional parameter space that separates stable $\mathbb{T}^1$ from invariant $\mathbb{T}^2$. In this curve (the Naimark–Sacker bifurcation curve), the ratio between the two frequencies of the $\mathbb{T}^2$, ω_s/ω_f, varies continuously along the curve. At any point with a rational ratio, $\omega_s/\omega_f = p/q$, a resonant horn emerges into the $\mathbb{T}^2$ region of the parameter space. The width of these resonant horns varies as $d^{(q-2)/2}$, where d is the distance from the curve. This scaling and the discussion to follow are valid for $q \geq 5$; the so-called soft resonances. For $q < 5$, the hard resonances, the situation is much more complicated and complete results are not yet available [14]. On our one-dimensional path, we do not observe any hard resonances and so we limit what follows to the soft resonances.

Near the Naimark–Sacker curve, on the $\mathbb{T}^2$ side, an invariant $\mathbb{T}^2$ exists. Outside horn regions, near the Naimark–Sacker curve, solutions are dense on the $\mathbb{T}^2$, leading to quasi-periodic flow with two incommensurate frequencies. On the horn boundary, a saddle-node bifurcation takes place on the $\mathbb{T}^2$, and inside the horn

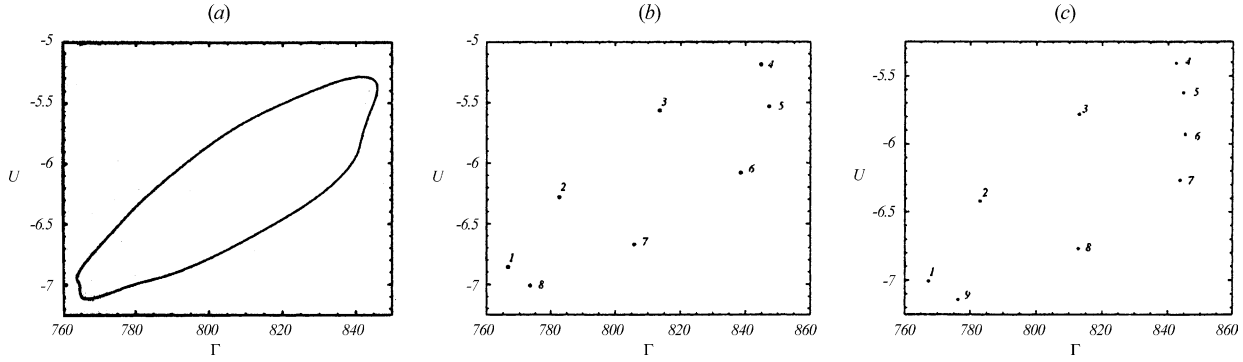

Fig. 13. Phase portraits for $Ra = 80$, $\omega_f = 30$, $e = 0.905$, $\Lambda = 10$ and $Ri = 280.48$ (a), 280.5 (b), 282 (c). For the locked cases, the order in which the trajectory passes through the Poincaré map is indicated.

a stable/unstable pair of limit cycle solutions exist on the $\mathbb{T}^2$. In the generic two parameter scenario, at large distance from the curve, the $\mathbb{T}^2$ may be destroyed. The Afraimovich–Shilnikov theorem [2] asserts three distinct scenarios: (i) breakdown due to some typical bifurcation of limit cycles, e.g. period doubling or subsequent Naimark–Sacker bifurcations; (ii) abrupt transition to chaos via the appearance of a homoclinic trajectory; (iii) breakdown due to the loss of smoothness, i.e. wrinkling of the $\mathbb{T}^2$. On our one-dimensional path, we have observed scenarios (i) and (iii).

The phase portrait shown in Fig. 13(a) corresponding to $Ri = 280.48$, is that of an invariant circle. The second frequency, $\omega_s \approx 3.8$, is incommensurate with $\omega_f = 30$. We have only been able to continue this branch down to $Ri = 280.46$, where $\omega_s = 3.896$. Increasing Ri, our one-dimensional path passes through various resonance horns. The first, a 1:8 locking, is encountered at $Ri = 280.49$ and extends to $Ri = 280.7$. The phase portrait in Fig. 13(b) shows this 1:8 locking at $Ri = 280.50$, where we have labeled the order in which the solution trajectory crosses the Poincaré section. Following an interval of quasi-periodicity at $Ri = 281.4$, the 1:9 horn is encountered (at $Ri = 281.0$, ghosting behavior near the 2:17 horn has been detected). The 1:9 horn extends to $Ri = 282$ and Fig. 13(c) shows the phase portrait at this Ri.

On leaving the 1:9 horn, the $\mathbb{T}^2$ displays evidence of having lost smoothness. Fig. 14 shows the phase portrait at $Ri = 282.1$ together with a zoom of the boxed region. The solution at this Ri is actually a limit cycle due to a 3:28 locking; as the resonance horn is very narrow, the transient approach to the limit cycle is very slow. The transient trajectory allows us to visualize the

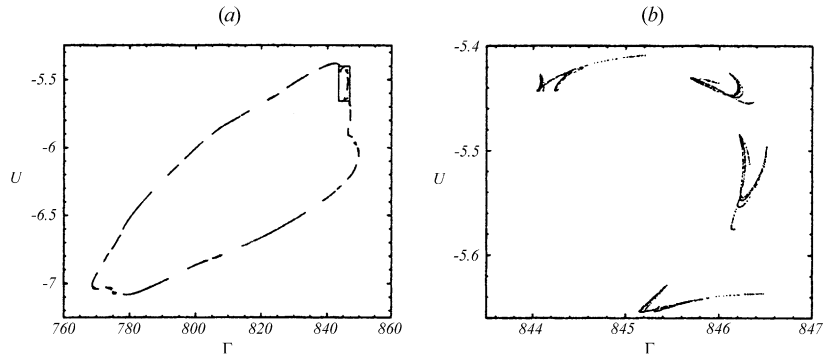

Fig. 14. (a) Phase portrait for $Ra = 80$, $\omega_f = 30$, $e = 0.905$, $\Lambda = 10$ and $Ri = 282.1$; (b) a zoom of the boxed region in (a).

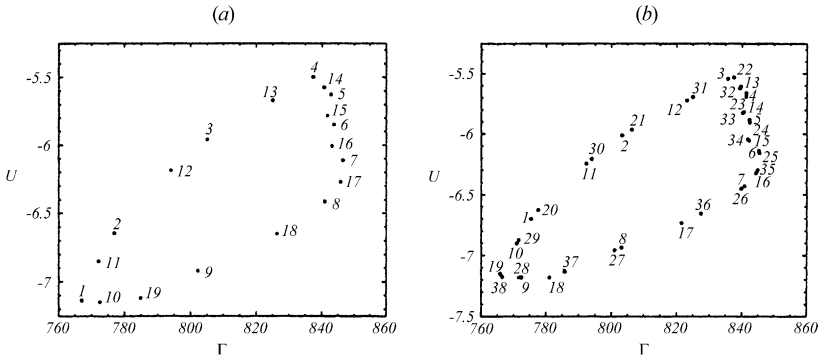

Fig. 15. Phase portraits for $Ra = 80, \omega_f = 30, e = 0.905, \Lambda = 10$ and $Ri = 282.4$ (a), and 282.5 (b). The order in which the trajectory passes through the Poincaré map is indicated.

underlying $\mathbb{T}^2$. It is clear that the $\mathbb{T}^2$ has lost smoothness, displaying the characteristic wrinkling observed in [11].

The 2:19 horn is entered on increasing Ri to 282.3. A phase portrait at $Ri = 282.4$ is shown in Fig. 15(a). The sequence of horns visited so far is as expected from their Farey tree structure; we began with 1:8, then 1:9, with a ghost of the 2:17 in between, then the 2:19, which is the widest horn between the 1:9 and 1:10. We also observed the wrinkling at the 3:28 between the 1:9 and 2:19. Now, inside the 2:19, at $Ri = 282.5$ the 2:19 limit cycle undergoes a period doubling to 4:38. In the range $282.5 \leq Ri \leq 282.7$, we have observed the 4:38 limit cycle. Fig. 15(b) shows the phase portrait at $Ri = 282.5$. This type of period doubling is one of the standard scenarios by which the $\mathbb{T}^2$ is destroyed according to the Afraimovich–Shilnikov theorem.

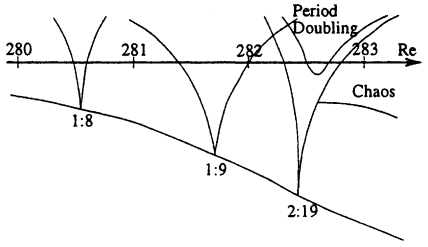

Fig. 16. Schematic representation of the one-dimensional path along the secondary branch.

Along our one-dimensional path, the period doubled region is exited and we re-enter the 2:19 region of the horn. A schematic representation of our path is shown in Fig. 16. On further increasing Ri, the 2:19 horn is exited and from this point on, the $\mathbb{T}^2$ becomes increasingly less smooth and eventually the flow is

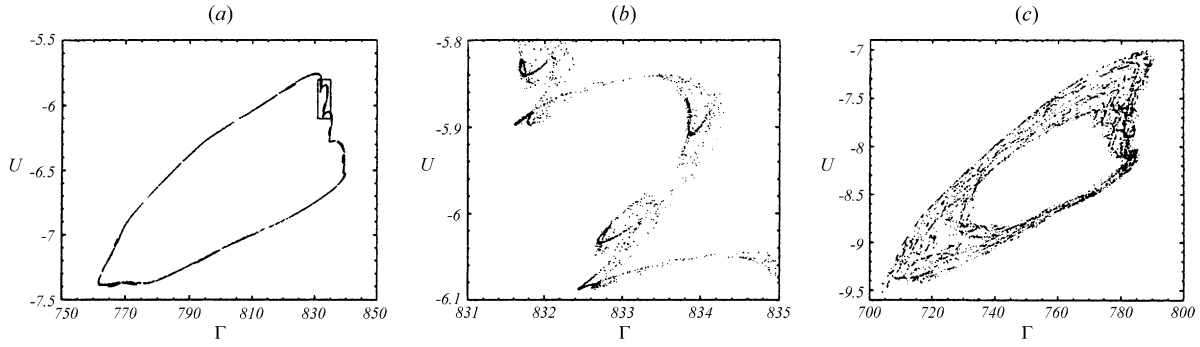

Fig. 17. Phase portraits for $Ra = 80, \omega_f = 30, e = 0.905, \Lambda = 10$. (a) $Ri = 283.1$, (b) a zoom of the boxed region in (a) and (c) $Ri = 285$.

chaotic. At $Ri = 283.1$, the wrinkling is illustrated in Fig. 17(a) together with a zoom in (b) and the phase portrait of a chaotic state at $Ri = 285$ is given in Fig. 17(c).

6. Summary and conclusions

We have studied a one-dimensional route in parameter space of a periodically forced flow with symmetry. As this parameter, *Ri*, is increased, the system undergoes a sequence of local and global bifurcations and becomes chaotic. The route to chaos obtained involves a new and convoluted symmetry breaking, involving heteroclinic, homoclinic and gluing bifurcations of $\mathbb{T}^3$.

An overall description of our one-dimensional path is schematically presented in Fig. 18. The solid curves correspond to stable $\mathbb{T}^1$, $\mathbb{T}^2$ and $\mathbb{T}^3$ solution branches which were encountered. The dashed curves connecting them are conjectured based on the properties of the stable solutions. The primary branch, consisting of S-invariant $\mathbb{T}^1$, undergoes a supercritical Naimark–Sacker bifurcation to an S-invariant $\mathbb{T}^2$. This is the generic scenario of a Z_2-symmetric Naimark–Sacker [14]. The resulting $\mathbb{T}^2$ is S-invariant, but obviously the solutions (trajectories) on it are not S-invariant by virtue that the two frequencies on the $\mathbb{T}^2$ are incommensurate. This $\mathbb{T}^2$ loses stability, but remains S-invariant as *Ri* is increased, and solution trajectories evolve to a $\mathbb{T}^3$.

Continuing the $\mathbb{T}^3$ branch to lower *Ri*, the branch ceases to exist at a heteroclinic bifurcation as it collides with two S-symmetrically related unstable $\mathbb{T}^2$; the $\mathbb{T}^3$ is S-invariant. Increasing *Ri*, the $\mathbb{T}^3$ becomes homoclinic to an S-invariant unstable $\mathbb{T}^2$, which we conjecture is the unstable $\mathbb{T}^2$ from the primary branch. The conjecture is based on the close similarities of the corresponding oscillatory flows on the stable $\mathbb{T}^2$ and the unstable $\mathbb{T}^2$ to which the $\mathbb{T}^3$ becomes homoclinic to. The secondary frequency, ω_s, is continuous between the two $\mathbb{T}^2$, further supporting this conjecture. At the homoclinic point, the $\mathbb{T}^3$ suffers a symmetry breaking gluing bifurcation. This is the only symmetry breaking bifurcation we have observed in this system. The importance of the Z_2 symmetry in the Taylor–Couette problem and its association with complex dynamics (e.g. homoclinic and Shilnikov bifurcations) was pointed out by [23], and was also reviewed in [22].

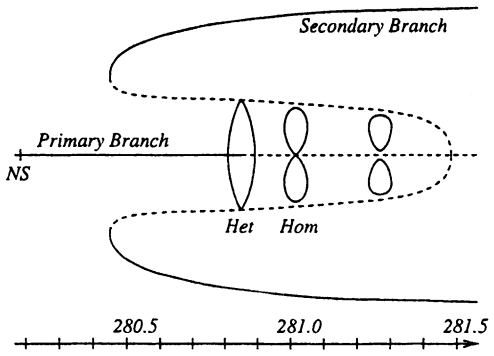

Fig. 18. Bifurcation diagram showing the primary, secondary and $\mathbb{T}^3$ branches; the dashed lines are the unstable branches.

Increasing *Ri* beyond a critical value, the $\mathbb{T}^3$ branch cannot be continued further and the flow evolves onto a $\mathbb{T}^2$ that is not S-invariant. In fact, there are two such $\mathbb{T}^2$ branches, symmetrically related, along which a standard (i.e. not influenced by symmetries) route to chaos via quasi-periodicity and locking in resonance horns and torus break-up is observed.

The three $\mathbb{T}^2$ to which the $\mathbb{T}^3$ are either heteroclinically or homoclinically asymptotic to the organizing centers of the dynamics of the $\mathbb{T}^3$. In fact, the $\mathbb{T}^3$ flows are essentially slow drifts, with VLF, between the unstable $\mathbb{T}^2$. Similar VLF states have also been observed experimentally [6,31,32] in an unforced Taylor–Couette flow with aspect ratio of order 10, as is the aspect ratio in our computations. Since their system was unforced, the VLF states manifested themselves as $\mathbb{T}^2$. Furthermore, those observed VLF states are reported to be axisymmetric modes of oscillation between the end-walls, even though the underlying flow is nonaxisymmetric [32]. We can reasonably expect that our axisymmetric $\mathbb{T}^3$ solutions, even if they are unstable to nonaxisymmetric disturbances continue to play an important role in the flow dynamics.

How are the various observed stable and unstable $\mathbb{T}^2$ connected? As *Ri* decreases along the secondary branch, ω_s increases from 3.2 to 3.9, getting close to ω_s values on the primary $\mathbb{T}^2$ and the $\mathbb{T}^3$ branches. This leads us to conjecture that the unstable $\mathbb{T}^2$ heteroclinic

to the $\mathbb{T}^3$ and the stable secondary $\mathbb{T}^2$ branch merge at a saddle-node bifurcation of $\mathbb{T}^2$ and cease to exist at lower *Ri*. This is the lowest co-dimension bifurcation consistent with the observed characteristics of the respective $\mathbb{T}^2$. All possible bifurcations of $\mathbb{T}^2$ is a subject that has not yet been exhaustively studied, but [7] describe the most likely scenarios associated with a real eigenvalue crossing the unit circle through ± 1 or the crossing of a pair of complex conjugate eigenvalues. Both the -1 and the complex conjugate crossing would introduce a new frequency, which is not the case in our system; the $+1$ crossing, since there is no symmetry involved, corresponds to a saddle-node.

We also conjecture that on increasing *Ri*, the unstable $\mathbb{T}^2$ associated with the $\mathbb{T}^3$ branch merge in a pitchfork bifurcation of $\mathbb{T}^2$. We have been able to observe the flows on (near) these three $\mathbb{T}^2$ and they are all very similar (see Figs. 9 and 10), so it is reasonable that at large enough *Ri*, they merge. The simplest bifurcation consistent with one symmetric and two symmetrically related $\mathbb{T}^2$ is the pitchfork.

To further clarify these conjectured connections between the stable and unstable $\mathbb{T}^2$, two tools are required: (i) the computation and continuation with parameter variation of unstable $\mathbb{T}^2$; (ii) a generalized Floquet analysis for $\mathbb{T}^2$.

Acknowledgements

This work was partially supported by DGICYT grant PB97-0685 and Generalitat de Catalunya grant 1999BEAI400103 (Spain), and NSF grants DMS-9706951, INT-9732637 and CTS-9908599 (USA).

References

[1] D. Ambruster, B. Nicolaenko, N. Smaoui, P. Chossat, Symmetries and dynamics for 2D Navier–Stokes flow, Physica D 95 (1996) 81–93.

[2] V.S. Anishchenko, M.A. Safonova, L.O. Chua, Confirmation of the Afraimovich–Shilnikov torus-breakdown theorem via a torus circuit, IEEE Trans. Circuits Syst. I 40 (1993) 792–800.

[3] T.B. Benjamin, Bifurcation phenomena in steady flows of a viscous fluid, Proc. R. Soc. Lond. A 359 (1978) 1–26.

[4] T.B. Benjamin, T. Mullin, Anomalous modes in the Taylor experiment, Proc. R. Soc. Lond. A 377 (1981) 221–249.

[5] H.M. Blackburn, J.M. Lopez, Symmetry breaking of the flow in a cylinder driven by a rotating endwall, Phys. Fluids 12 (2000) 2698–2701.

[6] F.H. Busse, G. Pfister, D. Schwabe, Formation of dynamical structures in axisymmetric fluid systems, in: Evolution of Spontaneous Structures in Dissipative Continuous Systems, Lecture Notes in Physics, Vol. m55, Springer, Berlin, 1998, pp. 86–126.

[7] A. Chenciner, G. Iooss, Bifurcation of invariant torus, Arch. Rat. Mech. Anal. 69 (1979) 109–198.

[8] P. Chossat, G. Iooss, The Couette–Taylor Problem, Springer, Berlin, 1994.

[9] K.A. Cliffe, J.J. Kobine, T. Mullin, The role of anomalous modes in Taylor–Couette flow, Phil. Trans. R. Soc. Lond. A 439 (1992) 341–357.

[10] K.A. Cliffe, T. Mullin, A numerical and experimental study of anomalous modes in the Taylor experiment, J. Fluid Mech. 153 (1985) 243–258.

[11] J.H. Curry, J.A. Yorke, A transition from Hopf bifurcation to chaos: computer experiments with maps in R^2, in: J.C. Martin, N.G. Markley, W. Perrizo (Eds.), The Structure of Attractors in Dynamical Systems, Springer Notes in Mathematics, Vol. 668, Springer, Berlin, 1978, pp. 48–66.

[12] P. Gaspard, Measurement of the instability rate of a far-from-equilibrium steady state at an infinite period bifurcation, J. Phys. Chem. 94 (1) (1990) 1–3.

[13] P. Glendinning, Bifurcations near homoclinic orbits with symmetry, Phys. Lett. A 103 (1984) 163–166.

[14] Y.A. Kuznetsov, Elements of Applied Bifurcation Theory, 2nd Edition, Springer, Berlin, 1998.

[15] A.S. Landsberg, E. Knobloch, Oscillatory bifurcation with broken translation symmetry, Phys. Rev. E 53 (1996) 3579–3600.

[16] J.M. Lopez, F. Marques, Dynamics of 3-tori in a periodically forced Navier–Stokes flow, Phys. Rev. Lett. 85 (2000) 972–975.

[17] J.M. Lopez, F. Marques, J. Sanchez, Oscillatory modes in an enclosed swirling flow, J. Fluid Mech. (2001), in press.

[18] J.M. Lopez, F. Marques, J. Shen, Endwall effects in a periodically forced centrifugally unstable flow, Fluid Dyn. Res. 27 (2000) 91–108.

[19] J.M. Lopez, J. Shen, An efficient spectral-projection method for the Navier–Stokes equations in cylindrical geometries. I. Axisymmetric cases, J. Comput. Phys. 139 (1998) 308–326.

[20] F. Marques, J.M. Lopez, Taylor–Couette flow with axial oscillations of the inner cylinder: Floquet analysis of the basic flow, J. Fluid Mech. 348 (1997) 153–175.

[21] F. Marques, J.M. Lopez, Spatial and temporal resonances in a periodically forced extended system, Physica D 136 (2000) 340–352.

[22] T. Mullin, Disordered fluid motion in a small closed system, Physica D 62 (1993) 192–201.

[23] T. Mullin, K.A. Cliffe, Symmetry breaking and the onset of time dependence in fluid mechanical systems, in: S. Sarkar (Ed.), Nonlinear Phenomena and Chaos, Adam Hilger, Bristol, 1986, pp. 96–112.

[24] J. Shen, Efficient spectral-Galerkin method. I. Direct solvers for second-and fourth-order equations by using Legendre polynomials, SIAM J. Sci. Comput. 15 (1994) 1489–1505.
[25] J. Shen, Efficient Chebyshev–Legendre Galerkin methods for elliptic problems, in: A.V. Ilin, R. Scott (Eds.), Proceedings of ICOSAHOM'95, Houston J. Math. (1996) 233–240.
[26] J. Shen, Efficient spectral-Galerkin methods. III. Polar and cylindrical geometries, SIAM J. Sci. Comput. 18 (1997) 1583–1604.
[27] J.L. Stevens, J.M. Lopez, B.J. Cantwell, Oscillatory flow states in an enclosed cylinder with a rotating end-wall, J. Fluid Mech. 389 (1999) 101–118.
[28] G.G. Stokes, On the effect of the internal friction of fluids on the motion of pendulums, Trans. Camb. Phil. Soc. 9 (1851) 8.
[29] J.W. Swift, K. Wiesenfeld, Suppression of period doubling in symmetric systems, Phys. Rev. Lett. 52 (1984) 705–708.
[30] J. van Kan, A second-order accurate pressure correction scheme for viscous incompressible flow, SIAM J. Sci. Stat. Comput. 7 (1986) 870–891.
[31] J. von Stamm, T. Buzug, G. Pfister, Frequency locking in axisymmetric Taylor–Couette flow, Phys. Lett. A 194 (1994) 173–178.
[32] J. von Stamm, U. Gerdts, T. Buzug, G. Pfister, Symmetry breaking and period doubling on a torus in the VLF regime in Taylor–Couette flow, Phys. Rev. E 54 (5) (1996) 4938–4957.
[33] A.Y. Weisberg, I.G. Kevrekidis, A.J. Smits, Delaying transition in Taylor–Couette flow with axial motion of the inner cylinder, J. Fluid Mech. 348 (1997) 141–151.